

Propagation Characteristics for UAVs Operating at Short Range and Low Altitude

Giselle M. Galvan-Tejada^{1, *}, Jorge E. Aviles-Mejia², Aldo G. Orozco-Lugo¹,
Luis A. Arellano-Cruz³, Ruben Flores-Leal¹ and Rogelio Lozano-Leal^{3, 4}

Abstract—Propagation mechanisms for short range, low altitude conditions are reviewed for their use in communications of unmanned aerial vehicles (UAVs). This study is based on measurements conducted in an obstacle-free area. The testbed is made up of a testing UAV (in particular a drone) and a set of four ground station terminals (GSTs) located in a football field; the antenna heights of radios (onboard the drone and GSTs) are equal to 1.4 m, and the maximum distance between them is 50 m. Under these conditions, a plane earth geometry is well suited, and therefore the two-ray propagation model is considered. Measurement results for a radial configuration of the drone with respect to a ground station follow the trend of this model, but with a shift, which is attributed to the scattering from the grass. Then, an adjusted two-ray model is proposed for which experiments report good results. For another configuration where the drone has different positions in a square area of 30×30 m and there are four ground stations in the corners of the square, the general trend of the power decay of measurement results follows this model, but in some positions a difference around it is found even for locations at the same distance drone-GTSS. This behavior is attributed to the interaction of the print circuit board to the radiation characteristics of the antenna used in the radios. Thus, this effect is also analyzed by simulations, whose results show a deformation of the antenna radiation pattern, concentrating the energy in a certain direction and reducing it in another.

1. INTRODUCTION

Nowadays, unmanned aerial vehicles (UAVs) are spreading for different applications around the world. These devices, commonly known as drones, have diverse designs, configurations, and capabilities, which make them candidates to be included into the forthcoming fifth-generation (5G) and beyond [1, 2]. An essential component of UAVs, operated either as a single device or as swarm of drones, is the communication technology used between devices (e.g., UAV-UAV, UAV-ground station). Basically, there are two types of communications components [2]: *control and non-payloads communication (CNPC)* and *payload communication*. In any case, these components use wireless technology, and therefore, it is important to study their propagation characteristics. Provided that UAVs usually fly over obstructions, it is a regular practice to assume that they present line-of sight (LOS) conditions (i.e., when the propagation path between transmitter and receiver is free of obstructions). Nevertheless, non-line-of-sight (NLOS) communications can be present as well, particularly when UAVs fly at low altitude in hilly zones or urban and suburban areas (in other words, NLOS conditions implies that natural or artificial obstructions can be present in the propagation path between terminals). Moreover,

Received 6 November 2019, Accepted 30 January 2020, Scheduled 5 March 2020

* Corresponding author: Giselle M. Galvan-Tejada (ggalvan@cinvestav.mx).

¹ Communications Section, Department of Electrical Engineering, Center for Research and Advanced Studies of IPN, Mexico City 07360, Mexico. ² XLIM Research Institute, UMR CNRS 7252, University of Limoges, Limoges 87032, France. ³ UMI LAFMIA Laboratory, Center for Research and Advanced Studies of IPN, Mexico City 07360, Mexico. ⁴ Universites de Technologie de Compiègne, CNRS UMR Heudiasyc-UTC, Compiègne 60203, France.

Tatar Mamaghani and Hong [3] pointed out that at low-altitude the UAV propagation channel presents small-scale Rician fading with a probabilistic path loss attenuation[†]. See [3, 5–7] for LOS or NLOS approaches taken for different examples of UAVs implementations.

The objective of this paper is to analyze the behavior of the received power levels (which is related to the path loss characteristics) for a short range, low altitude environment. The scenario considered consists of an outdoors obstruction-free zone, where a testing UAV (particularly a drone) is located at low altitude (less than 2 m) and within a relatively small area (a square of 30 × 30 m). The previous setup is relevant because there are applications of UAVs at low altitude like civil engineering [8], field crop phenotyping [9], delivery of some Internet of Things (IoT) services [10], monitoring of water quality [11], to mention just a few. Hence, results derived from our study could be of practical interest.

Then, for the characteristics of the scenario considered here, it could be in principle possible to adopt some electromagnetic propagation fundamentals used for short range wireless networks. For example, in microcellular mobile systems, the well-known two-slope propagation model is usually applied (i.e., a combination of two models with different power decay exponents), which considers the so-called breakpoint distance. This distance represents the border that divides two regions with different trends of the signal path loss (e.g., free space and two-ray models) and can be determined theoretically as a function of the wavelength and the heights of the antennas. On the other hand, the tendency of the path loss can also be approximated by experimental results through linear regression analysis as has been addressed for some situations where UAVs operate [8–11]. However, in our case, we have observed experimentally that a single slope model based on the two-ray model is a better fit. A similar result is recently reported by Qiu et al. [12], but for a suburban area where the UAVs are at low altitudes near metallic and concrete structures.

Thus, the paper is organized as follows. Some preliminary concepts like free space propagation, power decay, and two-ray model are addressed in Section 2. The description of the measurement campaigns, analysis of results, and propagation model are presented in Section 3. We find that depending on the relative position of the drone and ground stations, some received signals at the same distance present a variation around the propagation model, which is attributed to the interaction of the print circuit boards of radios and their corresponding antennas. From this observation, a study of this effect is included in this paper in Section 4. Concluding remarks are given in Section 5.

2. PRELIMINARY CONCEPTS

2.1. Free Space Propagation: A Starting Point

For an environment without obstructions in the direct path between transmitter and receiver, reflections due to natural or artificial objects (including soil), or any type of atmospheric absorption, it is said that there are *free space propagation* conditions. Mathematically, this situation is expressed by a model that relates the received power, P_r , as a function of the distance d between the end-to-end terminals and the operating frequency through the wavelength λ [4]

$$P_r = P_t g_t g_r \left(\frac{\lambda}{4\pi d} \right)^2 \quad (1)$$

where P_t is the transmission power in mW (and consequently P_r is also in mW); g_t and g_r are the transmitter and receiver antenna gains, respectively; and both λ and d are given in m. In this paper, the end-to-end terminals correspond to a drone (transmitter) and a set of receivers called *Ground Station Terminals* (GSTs), which are located at some fixed reference points.

2.2. Power Decay

In general terms, there is a relationship between P_r and d through a *power decay exponent* or *path loss exponent*, γ , and hence a particular power decay law can be derived. This rate of power decay is usually

[†] It is worth mentioning that the small-scale fading addressed in [3] is associated with an environment where there exists a set of random propagation paths produced by natural or artificial objects, and when there is a dominant path, the fading statistics follow a Rician distribution [4]. The random nature of this environment implies that the path loss attenuation is modeled in a probabilistic form instead of a deterministic approach.

seen as a slope. For example, in the case of the free space model given by Eq. (1), there is only one slope for which $\gamma = 2$.

Now, under certain circumstances, a single slope model does not adequately characterize the propagation conditions, which has been pointed out by different authors [13–16], so sometimes a two-slope model could work well. Basically, the two-slope model represents how a certain signal experiences two distinct power decay laws so forming two different propagation regions. The transition between the two regions occurs at the so-called *breakpoint distance*, d_{bp} , in such a way that for distances shorter than d_{bp} , one will find a certain value γ_1 for the path loss exponent, while for distances larger than d_{bp} , its value changes to γ_2 . A typical example of a scenario that presents this behavior is that of microcell systems [18, 19], which operate at short range provided that transmission takes place at relatively low power levels [20], and antennas of base stations are installed below roof height [13]. In these scenarios, it is common to have $\gamma_1 = 2$ provided that free space conditions are found close to base stations [22, 23], and γ_2 has major variability of values depending on specific characteristics of the scenario such as open area, density of buildings, street widths, and terrain conditions.

Here, the scenario under study presents conditions like that of microcellular systems, which are based on a plane earth geometry. Nevertheless, as discussed above, microcellular systems typically follow a two-slope propagation model, whereas as it will be shown later, our case is better suited to a single slope model, in particular based on the two-ray model.

2.3. Two-Ray Model

When heights of antennas are relatively low, a reflection in the ground occurs in such a way that the transmitted signal travels via two paths, the direct one and reflected one. This situation follows the *two-ray model* based on a plane earth geometry (which is the case of interest here) whose electric field is [4]:

$$E = E_d \left\{ 1 + \rho e^{-j\Delta\phi} \right\} \quad (2)$$

where $E_d = \sqrt{30P_t g_t}/d$ represents the electric field of the direct wave (i.e., for free space conditions); ρ is the ground reflection coefficient; and $\Delta\phi$ is the phase difference between both paths. This difference is given by

$$\Delta\phi = \frac{2\pi}{\lambda} \Delta R = \frac{2\pi}{\lambda} \left(\sqrt{d^2 + (h_t + h_r)^2} - \sqrt{d^2 + (h_t - h_r)^2} \right) \quad (3)$$

where ΔR is the length difference between the direct and reflected paths and is directly determined from a plane earth geometry for antenna heights of transmitter and receiver given as h_t and h_r , respectively. Now, for vertical polarization, corresponding to the testbed used here, the reflection coefficient contained in Eq. (2) is [17]:

$$\rho = \frac{(\epsilon_r - jx) \sin \psi - \sqrt{(\epsilon_r - jx) - \cos^2 \psi}}{(\epsilon_r - jx) \sin \psi + \sqrt{(\epsilon_r - jx) - \cos^2 \psi}} \quad (4)$$

where ϵ_r is the dielectric constant of the medium relative to that of free space; ψ is the incidence angle with respect to the ground; and the term $x = 18 \times 10^9 \sigma/f$ relates the ground conductivity σ given in S/m and the operational frequency f in Hz. Please note that ρ is a complex quantity, so it can also be expressed by its magnitude $|\rho|$ and phase θ , in such a way that Eq. (2) can be rewritten as

$$E = E_d \left\{ 1 + |\rho| e^{-j(\Delta\phi - \theta)} \right\}, \quad (5)$$

which can be substituted in the following expression that relates the received power and electric field [4]:

$$P_r = \left(\frac{E\lambda}{2\pi} \right)^2 \frac{g_r}{120}. \quad (6)$$

Under the assumption of grazing incidence angles, i.e., $\psi \rightarrow 0$, $\rho = -1$, then the expression for received power of the two-ray model can be simplified to

$$P_r = 4 P_t g_t g_r \left(\frac{\lambda}{4\pi d} \right)^2 \sin^2 \left(\frac{2\pi h_t h_r}{\lambda d} \right) \quad (7)$$

If $d \gg h_t, h_r$, Eq. (7) is reduced to

$$P_r = P_t g_t g_r \left(\frac{h_t h_r}{d^2} \right)^2 \quad (8)$$

which shows that $\gamma = 4$.

Now, provided that we are considering short range (less than 50 m) and low altitude flights (less than 2 m), the condition $d \gg h_t, h_r$ does not hold, and the general expression (5) substituted in Eq. (6) is a better approach than that of Eq. (8). Then, by doing that to get this model in terms of its received power, it is easy to show that:

$$P_r = \left(\frac{E_d \{1 + |\rho| e^{-j(\Delta\phi - \theta)}\} \lambda}{2\pi} \right)^2 \frac{g_r}{120}. \quad (9)$$

The resulting plot is shown in Fig. 1 in a logarithmic scale, where the free space model is also included for comparison purposes. In these models, experimental settings explained in Section 3.1 and considering $\epsilon_r = 3$ and $\sigma = 1 \times 10^{-3}$ S/m for a very dry ground [24] were used. As can be seen, the two-ray model introduces a pattern of notches and crosses between the two models (some examples of these crosses are marked as circles in Fig. 1), associated with the phase differences due to the contribution of both waves. In spite of this variability, however, the two-ray model follows the free space profile (i.e., the power decay law) up to the last crossing, where a breakpoint could be theoretically identified (in this case at 185.3 m, where mathematical expressions of both models are equal), and beyond that value they diverge.

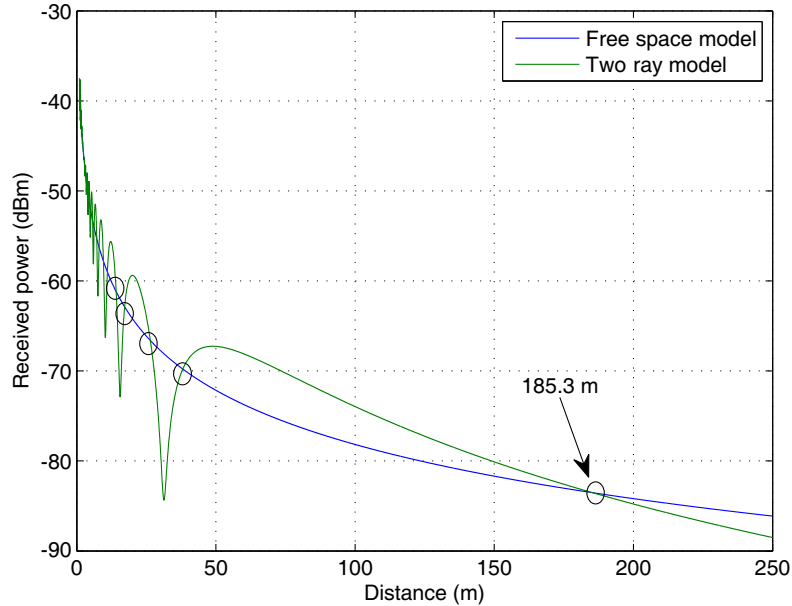


Figure 1. Plots of received power as a function of distance for free space and two-ray models.

3. MEASUREMENT CAMPAIGNS AND ANALYSIS OF RESULTS

3.1. General Settings

In order to determine a propagation model for short range and low latitude conditions, measurements were conducted in the football field of the Center for Research and Advanced Studies of IPN (Cinvestav-IPN), Mexico. This scenario was chosen in order to avoid reflecting objects, allowing us to observe the electromagnetic propagation phenomenon at low altitude and short range. In the same spirit, measurements were carried out on sunny or partially sunny weather conditions for all cases, so avoiding



Figure 2. Drone with a 2.4 GHz radio onboard.

atmospheric effects like rain or soil moisture, which can introduce additional attenuation in the propagation path associated with the scattering of the electromagnetic waves impinging on surfaces with water (rain drops, ground, etc.). The GSTs were implemented by using 2.4 GHz radios, whereas another radio with the same characteristics was installed onboard the drone (see Fig. 2). All these radios have a nominal transmission power of -2.5 dBm and omnidirectional right-angle vertical dipole Taoglas antennas GW.59.3153 with peak gain of 2.37 dBi [21], although 2.19 dBi was used as nominal gain. On the other hand, to avoid variations of signal due to multiple ground reflections near transmitter, the GSTs and drone were mounted over tripods of height equal to 1.4 m, which represents more than 10 times the operational wavelength (required condition for the two-ray model [22]). For all measurement points, 30 samples of received power were taken and their average calculated.

3.2. Experiment 1: Radial Measurements

Once the measurement settings have been stated, let us describe the first experiment and analyze its results. In this experiment, a total of 43 points were selected, and thus measurements were taken over a 50 m straight line using only one GST located at a fixed position and moving the drone in a radial way (see Fig. 3). Table 1 presents the average values (over the 30 samples) of the received power, P_{r_j} , for each selected distance, d_j , $j = 1, 2, \dots, N$, with $N = 43$ between the drone and the GST.

Additionally, these measurement results are graphically depicted in Fig. 4, where the free space and two-ray models are also included. As can be observed, experimental values approximate the form of the two-ray model. This behavior is also reported by Qiu et al. [12] for a low altitude suburban scenario (up to 45 m high) with metallic and concrete obstructions.

In our case, the measurement results seem to be right shifted with respect to the two-ray model, as can be appreciated in Fig. 4. This shift is attributed to the fact that the reflection is produced on grass in such a way that there is not a perfect specular reflection, so diffuse scattering could be present, producing a phase shift. To account for the observed phase shift, we propose to introduce a phase shifting factor in the received electric field as exposed in what follows.

3.3. Propagation Model

According to the measurement results analyzed in Section 3.2, we state that for UAVs operating in short range, low altitude and obstacle-free areas, two-ray based models are a better approach than the free space model[‡], and some considerations must be taken related to the reflecting surface. For example, in

[‡] Please note that for these conditions both models share the same power decay trend, but for some applications where a more detailed propagation model is required, the two-ray model is more appropriate.



Figure 3. Disposition of radios for a single 50 m straight line, drone (left), GST (right).

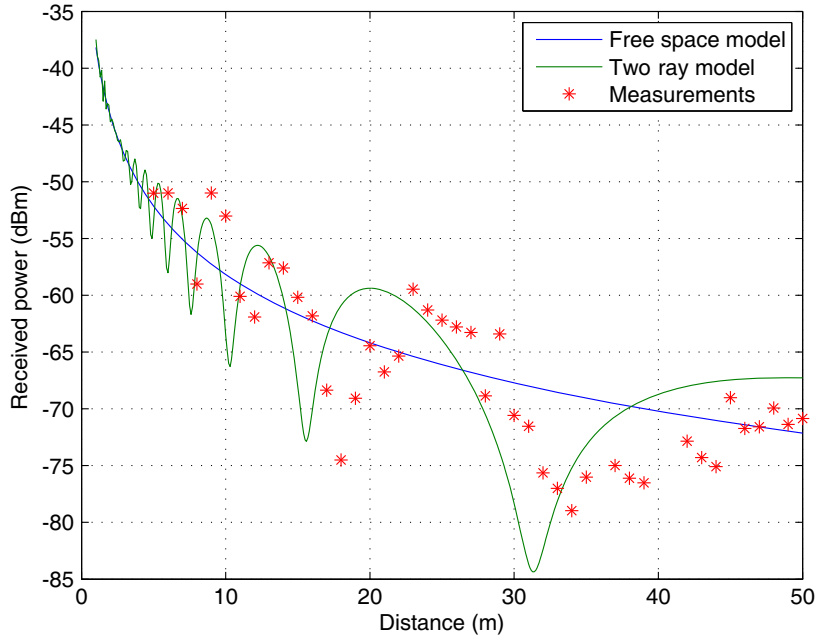


Figure 4. Measurement results of received power for a single 50 m straight line. Free space and two-ray models plots are also included for comparison purposes.

our grass testbed, we propose an *adjusted two-ray model* which includes a phase shifting factor $\alpha = \kappa \pi$ in the received electric field (5), in such a way that,

$$E_{adj} = E_d \left\{ 1 + |\rho| e^{-j(\Delta\phi - \theta - \alpha)} \right\}. \quad (10)$$

Note that $\alpha = 0$ corresponds to the two-ray model, so our adjusted model is more general. By

Table 1. Measurement results of the received power in Experiment 1.

Index j	Distance d_j (m)	Received Power P_{r_j} (dBm)	Index j	Distance d_j (m)	Received Power P_{r_j} (dBm)
1	5	-51.01284032	23	27	-63.27064425
2	6	-51	24	28	-68.86842934
3	7	-52.34931348	25	29	-63.41554974
4	8	-59.0067827	26	30	-70.58502149
5	9	-51	27	31	-71.54103083
6	10	-53.02782876	28	32	-75.65126308
7	11	-60.1043066	29	33	-77
8	12	-61.90787273	30	34	-78.97614046
9	13	-57.14048448	31	35	-76.02307763
10	14	-57.60312371	32	37	-75
11	15	-60.17725027	33	38	-76.11784566
12	16	-61.81401465	34	39	-76.51577846
13	17	-68.35626872	35	42	-72.85298299
14	18	-74.50513428	36	43	-74.29793323
15	19	-69.07553388	37	44	-75.09135487
16	20	-64.45133782	38	45	-69.01622446
17	21	-66.74413309	39	46	-71.72971235
18	22	-65.34943831	40	47	-71.58409162
19	23	-59.46924449	41	48	-69.93838755
20	24	-61.30579738	42	49	-71.37650895
21	25	-62.18775909	43	50	-70.85468055
22	26	-62.78354435	-	-	-

substituting Eq. (10) in place of E in Eq. (6), the received power is given as

$$P_{r_{adj}}(d; \alpha) = \left(\frac{E_d \{1 + |\rho| e^{-j(\Delta\phi - \theta - \alpha)}\} \lambda}{2\pi} \right)^2 \frac{g_r}{120}. \tag{11}$$

The previous equation represents our proposed model giving the received power as a function of distance. The phase shifting factor α is a parameter that can be chosen to obtain and adequately fit between the measurements and the model's predictions.

3.4. Optimization of the Phase Shifting Factor

The factor α must be selected in such a way as to optimize a suitable chosen fitting criterion, and we decide on the minimization of the sum of squares of the errors (that is, a least square approach) between the prediction of the proposed model and the measurements. Let us denote the received power measured at distance d_j as P_{r_j} ($j = 1, 2, \dots, N$), where the number of measurements is $N = 43$, according to our measurement campaign reported in Section 3.2 and summarized in Table 1. The error between the model-based received power $P_{r_{adj}}(d_j; \alpha)$ at distance d_j and the average measured value P_{r_j} at the same distance is given by

$$e_j(\alpha) = P_{r_{adj}}(d_j; \alpha) - P_{r_j}. \tag{12}$$

The nonlinear least squares criterion then reads (nonlinear because the relation between the received

power and α is nonlinear, see Equation (11))

$$\hat{\alpha} = \min_{\alpha} J(\alpha) = \min_{\alpha} \sum_{j=1}^N e_j^2(\alpha) \quad (13)$$

where $J(\alpha)$ stands for the objective function, and $\hat{\alpha}$ stands for the optimum value. Fig. 5 shows the normalized (with respect to the maximum) value of $J(\alpha)$ as a function of κ (remember that $\alpha = \kappa \pi$). Note that $J(\kappa) = J(\kappa + 2)$, that is, $J(\kappa)$ is a periodic function with period equal to 2 because it enters as the argument of the exponential in Equation (11). Hence, the search interval for κ is limited to that selected in the figure. By direct function evaluation to two decimal places of precision, we find that $\hat{\kappa} = 1.75$, as can be graphically observed in Fig. 5.

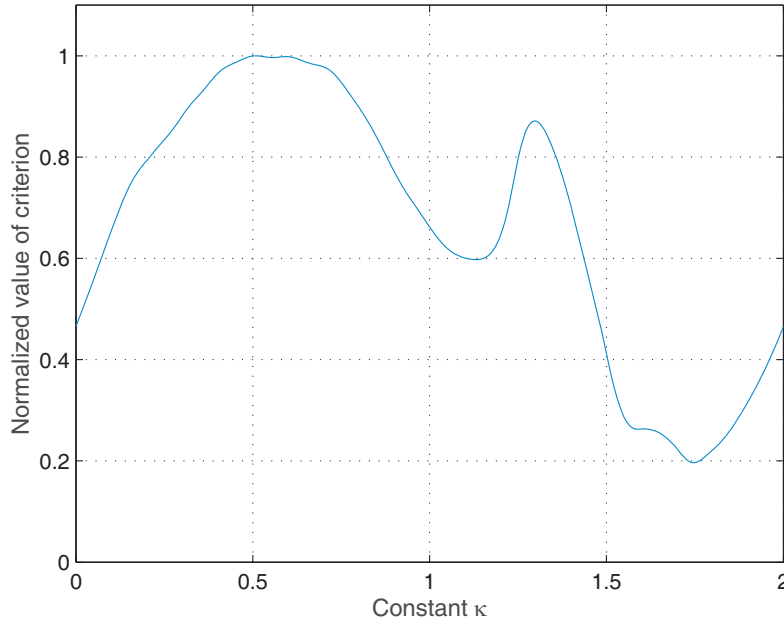


Figure 5. Normalized value of the objective function for different values of κ .

The optimum value $\hat{\kappa}$ of κ is so used to obtain $\alpha = 1.75 \pi$ which is then entered in the adjusted two-ray model of Eq. (11). Thus, we obtain the plot shown in Fig. 6, where the two-ray and free space models are also included for reference. As can be seen, there exists a good agreement between the proposed model and experimental results.

It is worth pointing out that the propagation model presented in Section 3.3 is valid for short ranges starting around 5 m. For shorter ranges, further analysis and measurement campaigns need to be conducted. This model could be tested for longer distances, for which new measurement campaigns are of course needed to have a comparison base and, if it is the case, carry out possible modifications. In addition, in a future study, it would be worth considering some interesting insights of the orbital angular momentum (OAM) concept as given in [25], which could be useful for extending the range of UAVs operating in wireless communications for 5G and beyond.

3.5. Experiment 2: Measurements in a Square Area

In a second measurement campaign, four radios were used as GSTs located in a regular disposition forming a 30×30 m square as shown in Fig. 7. Their geographical coordinates were taken using a Garmin GPS model GPSMAP 64s and are given in Table 2. The drone was moved according to positions marked as A, B, C, etc. in Fig. 7.

The results obtained from this experiment are displayed in Fig. 8, where for each location, A, B, C, etc. there are four distances drone-GST_{*i*}, with $i = 1, 2, 3, 4$ and therefore four mean values of received

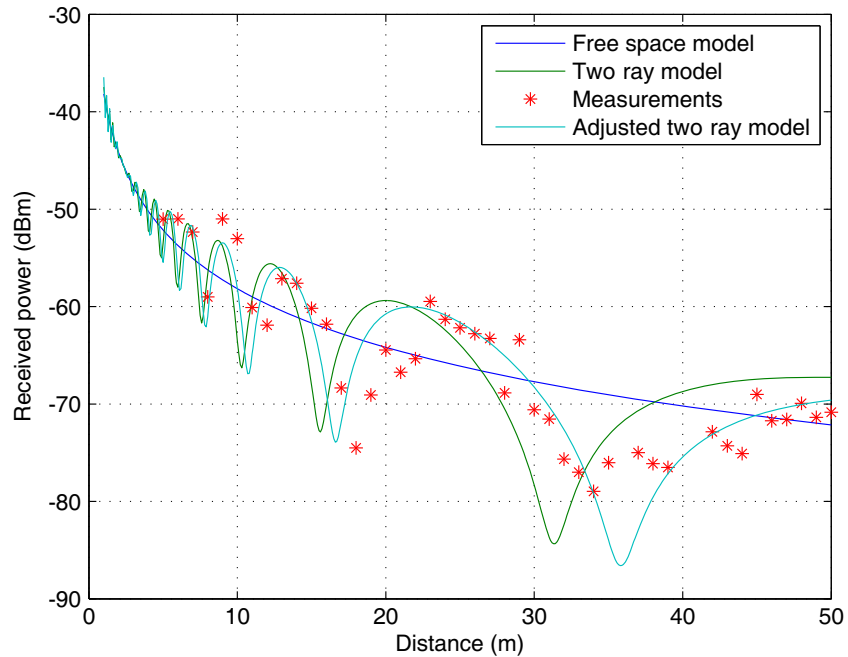


Figure 6. Comparison of the received power levels for the adjusted two-ray model and measurement results at different distances of Experiment 1. Free space and two-ray models plots are also included as reference.

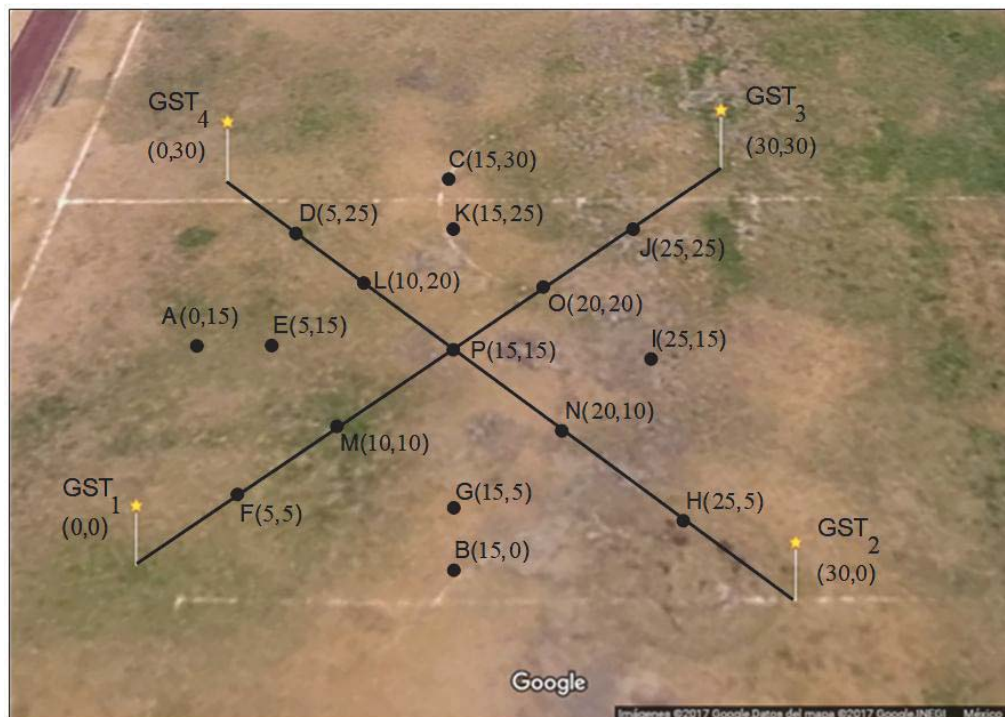


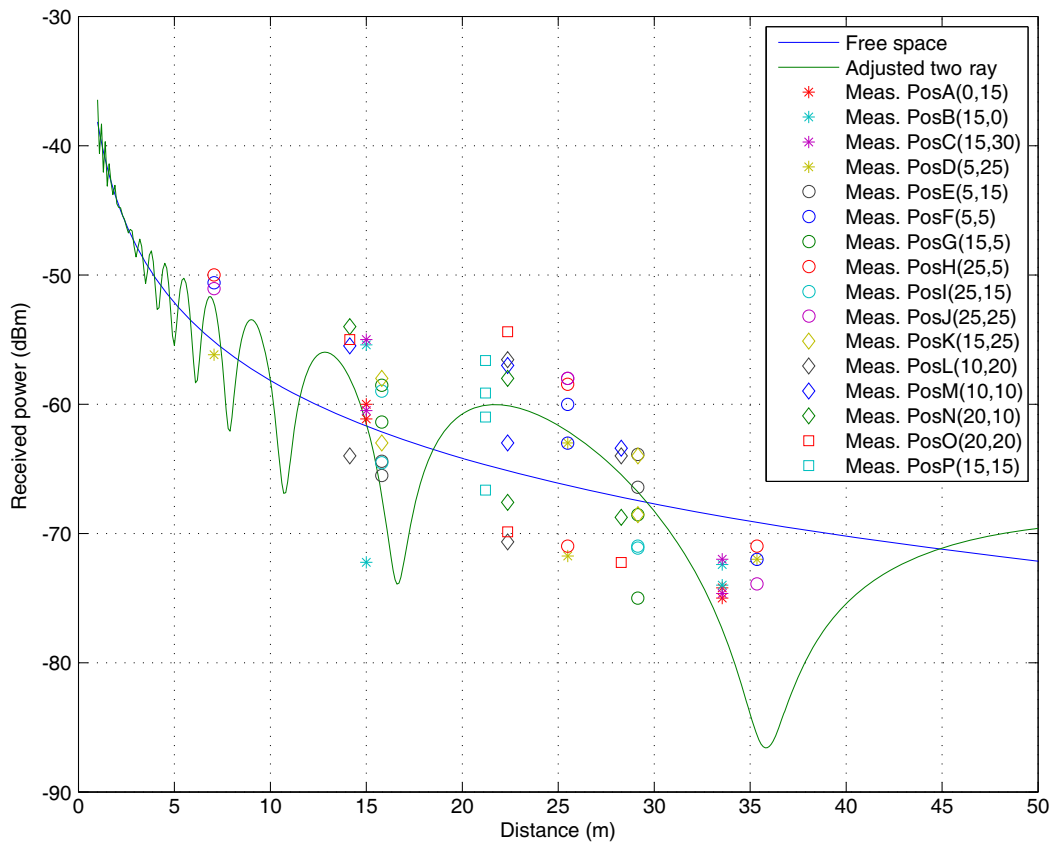
Figure 7. Positions of measurements.

power. Theoretical plots for free space and adjusted two-ray models are also included for comparison purposes. As can be appreciated, although the general trend of the power decay for these measurements follows the adjusted two-ray model, experimental results fluctuate around it. We also observe that some

Table 2. Geographical coordinates for GSTs.

GST	Latitude	Longitude
1	19°30'44.2" N	99°07'46.1" W
2	19°30'45.0" N	99°07'45.5" W
3	19°30'45.6" N	99°07'46.4" W
4	19°30'44.9" N	99°07'46.9" W

results present certain separation at the same distance. For example, at the center of the area, i.e., position P, with a distance of 21.21 m to each GST, a difference of 10 dB between the highest and lowest received powers is noted. This behavior can be attributed, among other factors, to the relative position of antennas in the printed circuit boards (PCBs) of the radios of GSTs and that of the drone, which influences the radiation characteristics of antennas. An analysis of this effect is exposed below in Section 4.

**Figure 8.** Measurement results of received power in a square area. Free space and adjusted two-ray models plots are also included for comparison purposes.

4. EFFECTS OF THE PRINT CIRCUIT BOARD TO THE ANTENNA RADIATION

As mentioned in Section 3.5, there are some positions in the second configuration of the measurement campaigns where a certain variation of the received power around the adjusted two-ray model is observed, which is related to the effect of the PCB to the antennas radiation characteristics. In particular, we note that for a given position of the drone where the distances drone-GST_{*i*} are equal,

the relative orientation of their PCBs introduces different levels of received power at the GSTs. This behavior was also pointed out in [26] for wireless sensor networks.

In order to test this effect, measurements of received power were carried out between a couple of radios separated by a fixed distance of 10 m (see Fig. 9), but for different horizontal angles, φ . This was done by rotating the drone in steps of 10 degrees over the center of its tripod and taking as a reference $\varphi = 0^\circ$ when both antennas have the shortest separation according to Fig. 10. Results of these measurements are shown in Fig. 11. As can be seen, as φ is increased, P_r is reduced up to $\varphi = 180^\circ$, where there is a 4 dB decrease in the received power relative to the reference of $\varphi = 0^\circ$. After this point, the levels of received power increased up to the value of -51 dBm for $\varphi = 350^\circ$.

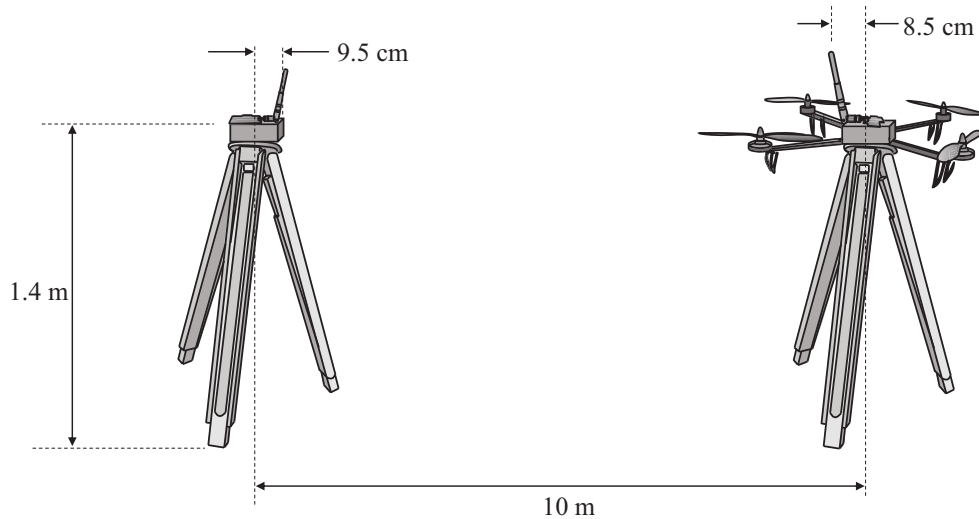


Figure 9. Configuration used to test the effect of circuit board on the radiation pattern. Left, GST, right, drone.

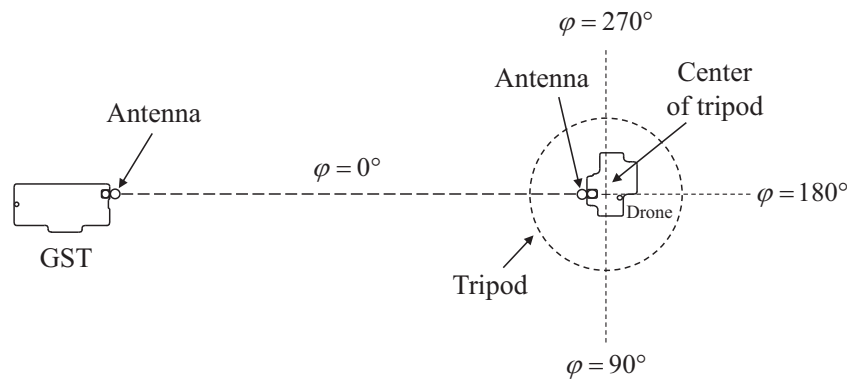


Figure 10. Superior view of printed circuit boards of both radios illustrating horizontal angles (e.g., $\varphi = 0^\circ$ corresponds to the shortest separation between antennas).

Then, from these observations, simulations of the antenna radiation pattern were carried out using the CST Microwave Studio simulator to test the effect of the PCB on it, where the PCB was considered as a Perfect Electric Conductor (PEC). In order to have a comparison base, first of all, we simulated the antenna alone (i.e., without PCB). In this case, we obtained a very regular omnidirectional pattern with a maximum gain of 1.611 dBi, as can be seen in Fig. 12. It is worth mentioning that the value of 2.37 dBi specified in [21] represents the peak gain, and it could not necessarily be at the horizontal plane (in fact, we had already reported a measured gain of 2.2 dBi [27] for a vertical angle relatively near to the horizontal plane).

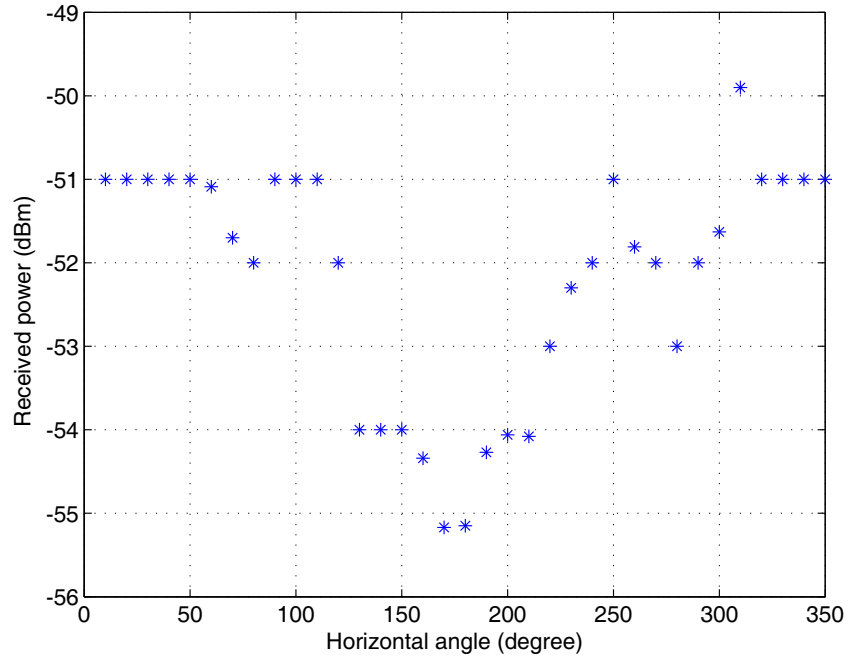


Figure 11. Mean received power at the GST as a function of the horizontal angle φ of the drone.

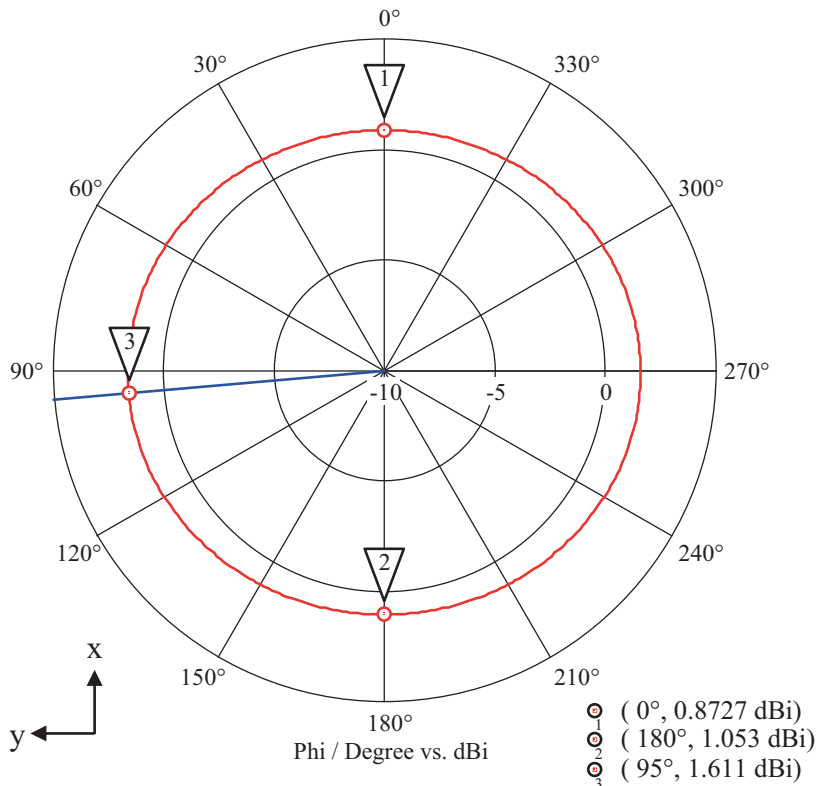


Figure 12. Simulation results of the horizontal radiation pattern of the antenna used in the drone without its PCB.

After that, simulations were carried out for the antenna with its PCB. Results are depicted in Fig. 13 for a 3D visualization and Fig. 14 for the horizontal plane. Fig. 15 is a superior view of the antenna and its PCB, which is presented here for reference of the results given in Fig. 14. As can be

seen, the presence of the PCB deforms the radiation pattern, with a minimum gain of -0.6446 dBi at 191° (i.e., near 180°) and a maximum of 1.073 dBi at 258° . This non-regular shape of the radiation pattern can be attributed to the disposition of antenna relative to the PCB, which does not have a

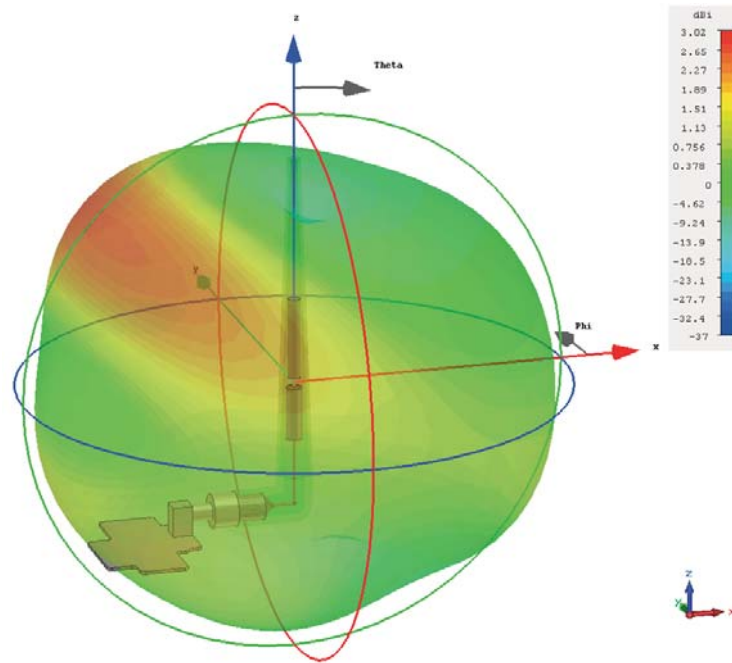


Figure 13. Simulation results of the 3D radiation pattern of the antenna used in the drone with its PCB.

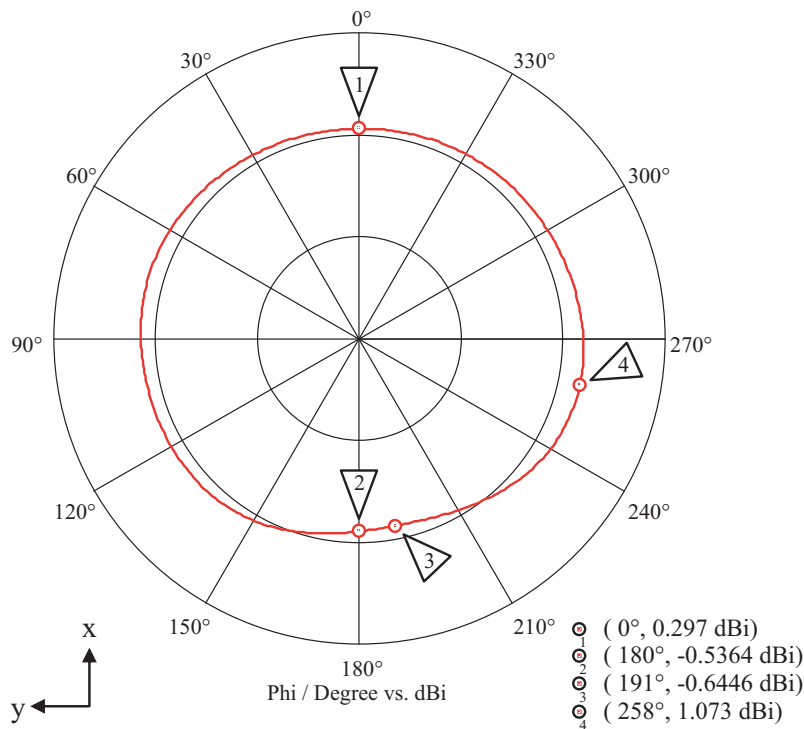


Figure 14. Simulation results of the horizontal plane of the radiation pattern of the antenna used in the drone with its PCB.

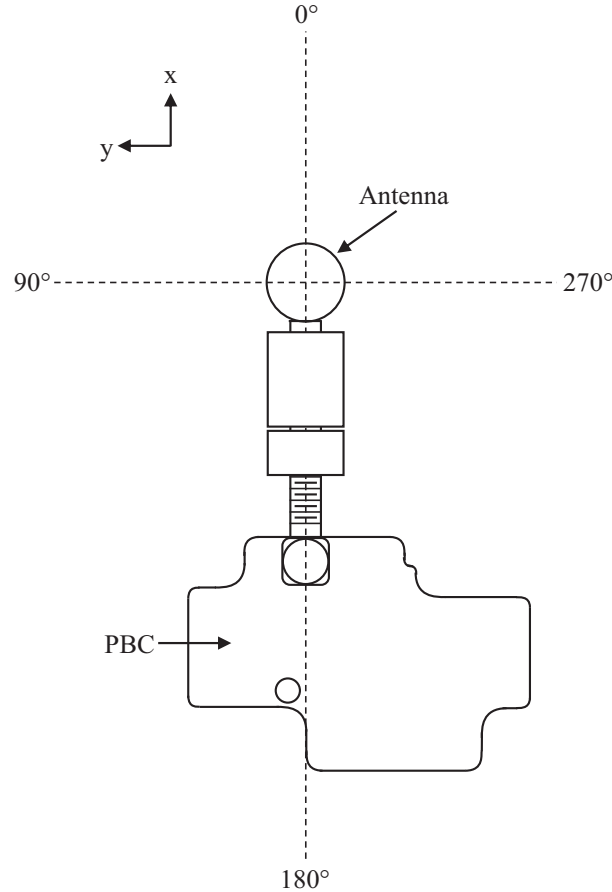


Figure 15. Superior view of the PCB and the antenna used in the drone.

regular shape either, as shown in Fig. 15. Regarding the difference of gains for angles of $\varphi = 0^\circ$ and $\varphi = 180^\circ$, it is around 0.83 dB. The smaller difference obtained by simulations than results given in Fig. 11 is because simulations consider an idealized model both for antenna and PCB, and to reduce computational load, no electronic components were included. In any case, as we stated, the objective of these simulations is to observe the effect of the PCB on the radiation pattern, so we can say that it acts as a reflector (because its separation distance is around $\lambda/4$ from the dipole arm) concentrating the energy in a direction and reducing it in another, which affects the levels of received power depending on the relative angle between both radios.

Derived from this analysis, it is important to point out that the effect of PCB on the radiation characteristics of antennas should be included in variables g_t and g_r of the propagation model for a practical implementation. In particular, the drone orientation determines the relative angle between it and a GST and consequently a variation of received energy in a certain direction.

5. CONCLUSION

An analysis of propagation mechanisms for short range, low altitude wireless communications for unmanned aerial vehicles was presented in this paper. The two-ray propagation model was studied as a candidate for the scenario under study. From radial measurements conducted in a testbed under outdoors obstructions-free conditions, we observed that this model could be useful for the whole range of measurements between 5 and 50 m. Experimental results were in good agreement with this model, and only an adjustment in the phase was necessary. Later, field measurements were carried out in the testbed using four ground station terminals positioned in the corners of a square of 30×30 m and for different locations of the drone. Due to some peculiar observations on the levels of received power, the

effect of the printed circuit board on the radiation pattern of antennas was also reviewed. Indeed, it behaves as reflector of the signal radiated by the antenna concentrating the energy towards a certain direction and reducing it in another. Thus, this effect can impact the signal received by some ground station terminals depending on the relative orientation and horizontal angle formed between the radios involved. Finally, it is worth mentioning that this study can be useful for some missions of UAVs that require knowledge of the received power levels. In fact, a position location algorithm based on received signal strength (where the propagation model studied here will be used) is currently being evaluated to be proposed in a future correspondence.

REFERENCES

1. Li, B., F. Zesong, and Y. Zhang, "UAV communications for 5G and beyond: Recent advances and future trends," *IEEE Internet of Things Journal*, Vol. 6, No. 2, 2241–2263, April 2019.
2. Zeng, Y., Q. Wu, and R. Zhang, "Accessing from the sky: A tutorial on UAV communications for 5G and beyond," submitted to *Proceedings of the IEEE*.
3. Tatar Mamaghani, M. and Y. Hong, "On the performance of low-altitude UAV-enabled secure AF relaying with cooperative jamming and SWIPT," *IEEE Access*, Vol. 7, 153060–153073, October 2019.
4. Parsons, J. D., *The Mobile Radio Propagation Channel*, John Wiley & Sons, 1992.
5. Dehghan, S. M. M. and H. Moradi, "A geometrical approach for aerial cooperative obstacle mapping using RSSI observations," *RSI/ISM International Conference on Robotics and Mechatronics*, 197–202, October 2014.
6. Simunek, M., F. Pérez Fontán, and P. Pechac, "The UAV low elevation propagation channel in urban areas: Statistical analysis and time-series generator," *IEEE Transactions on Antennas and Propagation*, Vol. 61, No. 7, 3850–3858, July 2013.
7. Virone, G., A. M. Lingua, M. Piras, A. Cina, F. Perini, J. Monari, F. Paonessa, O. A. Peverini, G. Addamo, and R. Tascone, "Antenna pattern verification system based on a micro Unmanned Aerial Vehicle (UAV)," *IEEE Antennas and Wireless Propagation Letters*, Vol. 13, 169–172, 2014.
8. Siebert, S. and J. Teizer, "Mobile 3D mapping for surveying earthwork projects using an Unmanned Aerial Vehicle (UAV) system," *Automation in Construction*, Vol. 41, 1–14, 2014.
9. Sankaran, S., L. R. Khot, C. Zúiga Esponzoza, et al., "Low-altitude, high resolution aerial imaging systems for row and field crop phenotyping: A review," *European Journal of Agronomy*, Vol. 70, 112–123, 2015.
10. Motlagh, N. H., T. Taleb, and O. Arouk, "Low-altitude unmanned aerial vehicles-based internet of things services: Comprehensive survey and future perspectives," *IEEE Internet of Things Journal*, Vol. 3, No.6, 899–922, December 2016.
11. Koparan, C., A. B. Koc, C. V. Privette, and C. B. Sawyer, "In situ water quality measurements using an Unmanned Aerial Vehicle (UAV) system," *Water*, Vol. 10, No. 3, 264, 2018.
12. Qiu, Z., X. Chu, C. Calvo-Ramirez, C. Briso, and X. Yin, "Low altitude UAV air-to-ground channel measurement and modeling in semiurban environments," *Wireless Communication and Mobile Computing*, Vol. 2017, 1–11, 2017.
13. Green, E. and M. Hata, "Microcellular propagation measurements in an urban environment," *IEEE International Symposium on Personal, Indoor and Mobile Radio Communications*, 324–328, 1991.
14. Xia, H. H., H. L. Bertoni, L. R. Maciel, A. Lindsay-Stewart, and R. Rowe, "Radio propagation characteristics for line-of-sight microcellular and personal communications," *IEEE Transactions on Antennas and Propagation*, Vol. 41, No. 10, 1439–1447, October 1993.
15. Perera, S. C. M., A. G. Williamson, and G. R. Rowe, "Prediction of breakpoint distance in microcellular environments," *Electronics Letters*, Vol. 35, No. 14, 1135–1136, July 1999.
16. Masui, H., T. Kobayashi, and M. Akaike, "Microwave path-loss modeling in urban line-of-sight environments," *IEEE Journal on Selected Areas in Communications*, Vol. 20, No. 6, 1151–1155, August 2002.

17. Jordan, E. C. and K. G. Balman, *Electromagnetic Waves and Radiating Systems*, Prentice-Hall, 2nd Edition, 1968.
18. McFarlane, D. A. and S. T. S. Chia, "Microcellular mobile radio systems," *British Telecom Technology Journal*, Vol. 8, No. 1, 79–84, January 1990.
19. Green, E., "Radio link design for microcellular systems," *British Telecom Technology Journal*, Vol. 8, No. 1, 85–96, January 1990.
20. Xia, H. H., H. L. Bertoni, L. R. Maciel, A. Lindsay-Stewart, and R. Rowe, "Microcellular propagation characteristics for personal communications in urban and suburban environments," *IEEE Transactions on Vehicular Technology*, Vol. 43, No. 3, 743–752, August 1996.
21. <http://www.taoglas.com/product/gw-59-2-45-8ghz-3dbi-dipole-antenna-rp-smam-hinged/>.
22. Feuerstein, M. J., K. L. Blackard, T. S. Rappaport, S. Y. Seidel, and H. H. Xia, "Path loss, delay spread, and outage models as functions of antenna height for microcellular system design," *IEEE Transactions on Vehicular Technology*, Vol. 43, No. 3, 487–498, August 1994.
23. Blackard, K. L., M. J. Feuerstein, T. S. Rappaport, S. Y. Seidel, and H. H. Xia, "Path loss and delay spread models as functions of antenna height for microcellular system design," *IEEE 42nd Vehicular Technology Conference*, 333–337, May 1992.
24. Recommendation ITU-R P.527-4, "Electrical characteristics of the surface of the Earth," *International Telecommunication Union, Radiocommunication Sector of ITU, P Series, Radiowave Propagation*, 1–19, June 2017.
25. Sjöholm, J. and K. Palmer, "Angular momentum of electromagnetic radiation: Fundamental physics applied to the radio domain for innovative studies of space and development of new concepts in wireless communications," Diploma Thesis, Uppsala School of Engineering and Department of Astronomy and Space Physics, Uppsala University, Sweden, 1–186, May 2007.
26. Lymberopoulos, D., Q. Lindsey, and A. Savvides, "An empirical characterization of radio signal strength variability in 3-D IEEE 802.15.4 networks using monopole antennas," *European Workshop on Wireless Sensor Networks*, 326–341, 2006.
27. Galvan-Tejada, G. M., R. Flores-Leal, F. Sanchez-Gomez, and V. Barrera-Figueroa, "On the importance of the vertical radiation pattern on simulations of WSNs," *2016 13th International Conference on Electrical Engineering, Computing Science and Automatic Control (CCE)*, 1–6, September 2016.